

# Chapter 2

## Freely Accelerating Impact into Cornstarch and Water Suspensions

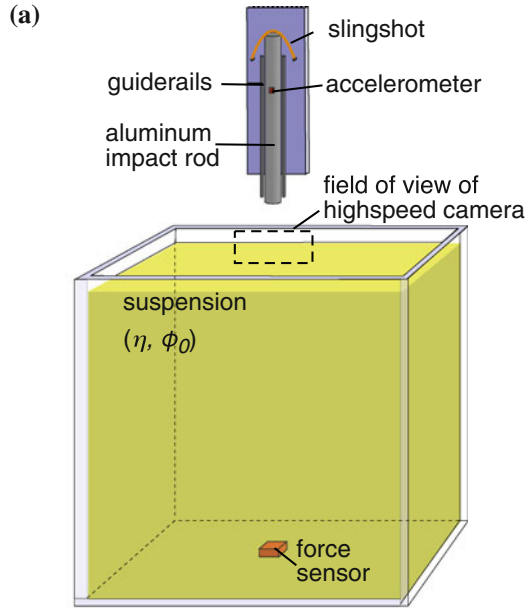
### 2.1 Introduction

While the experiments described in the previous chapter primarily focused on rheological measurements of dense suspensions, the focus of this thesis is surface impact. As a number of studies have shown, liquids and granular media typically flow around and provide little resistance to intruding objects [1–11], while suspensions can provide normal stresses that are large enough to support a person running across their surface. As discussed previously, this impact response has been attributed to suspension response under shear, linking it to hydrodynamic interactions [12–17] or a combination of granular dilation and jamming [18–24], but neither of these mechanisms alone can produce enough normal stress to explain impact. In this chapter, we describe a series of experiments designed specifically to study impact into dense suspensions. With techniques ranging from high-speed videography to embedded force sensing and X-ray imaging, we capture the detailed dynamics of the impact process as a metal rod strikes the surface of a dense cornstarch and water suspension. The data reveal that the impactor motion causes the rapid growth of a solid-like region directly below the impact site. These findings are in agreement with von Kann et al. but we go one step further by showing that this is mediated by “solidification fronts” and that no boundaries are necessary for the suspension to provide large normal stresses. Instead, as this solid moves and grows, it pulls on the surrounding suspension creating a quickly growing peripheral flow. Using the concept of added mass, we make a model that relates the sudden extraction of the impactors momentum to the growth of this flowing solid/peripheral region.

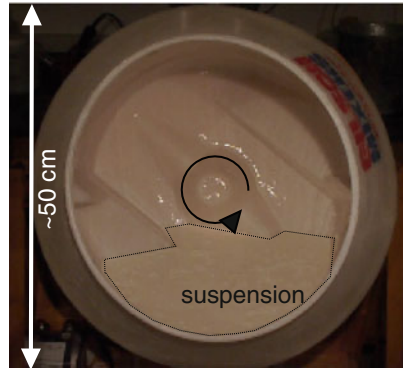
### 2.2 Experimental Setup

In Fig. 2.1a we show a schematic of the experimental apparatus. An aluminum rod (mass  $m_r = 0.368$  kg, radius  $r_r = 0.93$  cm) is shot into the surface of a cornstarch and water suspension by gravity or by slingshot. Vertical motion is maintained by

**Fig. 2.1 a** Freely accelerating impact experiment. An aluminum rod ( $r_r = 0.93$  cm,  $m_r = 0.368$  kg) is accelerated toward the surface of a cornstarch and water suspension (suspending liquid viscosity  $\eta$ , packing fraction  $\phi_0$ , fill height  $H$ ) via gravity or a slingshot. A high-speed camera focused on the region indicated in the figure tracks the rod to measure the impact velocity  $v_0$ . An embedded accelerometer measures the rod's instantaneous acceleration  $a_r$ . Directly below the impact site, a force sensor records any stress transmission through the suspension to the container bottom. **b** Preparing  $\sim 20$  L of cornstarch and water suspension with a cement mixer



(b)



gently cradling the rod between stainless steel guide rails. A lightweight, miniature accelerometer (Omega ACC104A) housed inside the rod is connected to a computer via USB data acquisition interface (labVIEW USB-6009) and records the rod's acceleration in real time at a data rate of 24,000 samples per second. As the rod hits the surface, a high speed camera (Phantom v9.1, Vision Research) records video (in the region indicated in the figure) at a typical frame rate of 10,000 frames per second. A laser trigger just above the suspension surface (not shown in the figure) initiates the camera. To measure any stress transmission to the container bottom, we place a high-speed force sensor (DLC101-10, DLC101-50, DLC101-50, or DLC101-500)

in a waterproof container directly beneath the rod (like the accelerometer, this sensor is also connected to the USB interface recording at 24,000 samples per second).

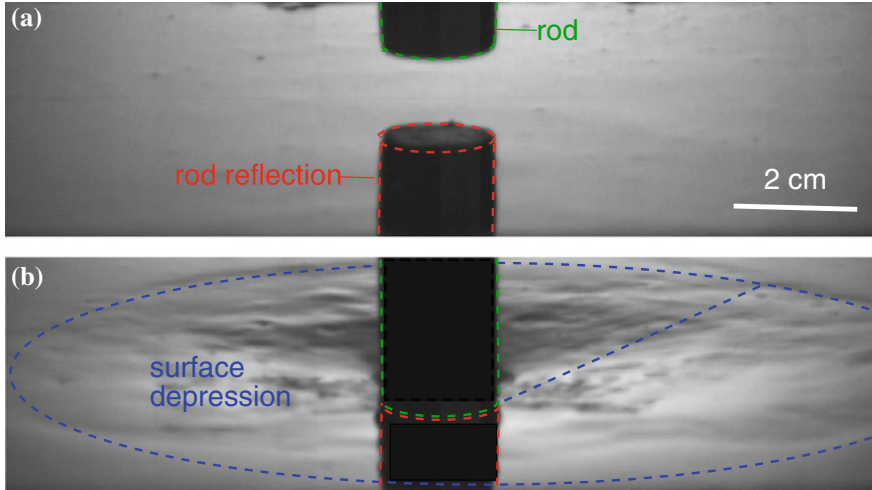
The cornstarch and water suspension is characterized by its packing fraction  $\phi_0$ , the suspending liquid viscosity  $\eta$ , the suspending liquid surface tension  $\sigma$ , and the fill height  $H$ . The first step in preparing the suspensions involves creating a suspending liquid with the desired viscosity. This is achieved by mixing tap water and glycerin (McMaster Carr 3190K293) with a wire whisk. We then measure the viscosity of this mixture with a capillary viscometer (Cannon Instrument Company, ratings 50–400). After measuring the suspending liquid viscosity, we extract  $\sim 25$  mL and measure the density with a volumetric measurement from a graduated cylinder and a mass measurement from a scale. (For these experiments, we do not density match the suspending liquid as the sheer volume required makes it prohibitively expensive. We prevent suspension settling by continually relayering the suspension throughout the day with a garden shovel.) We determine the necessary mass  $M_{cs}$  of cornstarch by first deciding on the desired packing fraction  $\phi_0$  and then using the equation

$$M_{cs} = \frac{\rho_{cs}}{\rho_l} M_l \frac{\phi_0}{1 - \phi_0}, \quad (2.1)$$

where  $M_l$  is the total mass of the suspending liquid and  $\rho_{cs}$  is the specific gravity of the cornstarch particles (i.e. the density of the material itself, not the perceived density of the powder plus air). The value for  $\rho_{cs}$  varies throughout the literature from about 1.55 [21] to 1.68 [25]; here, we do not make any measurements ourselves, but instead use a value in the middle of this range  $\rho_{cs} = 1.59$  [19]. We measure the total mass of cornstarch with a scale and then slowly added it into the suspending liquid in an industrial cement mixer, as in Fig. 2.1b. We used the cement mixer because the thickening behavior of the suspension makes it extremely difficult to mix “by hand”. Adding the cornstarch slowly prevents unwanted clumping and the formation of air bubbles in the suspension. Once all of the cornstarch is added, we let the mixer run for approximately one half hour until the suspension consistency is highly uniform.

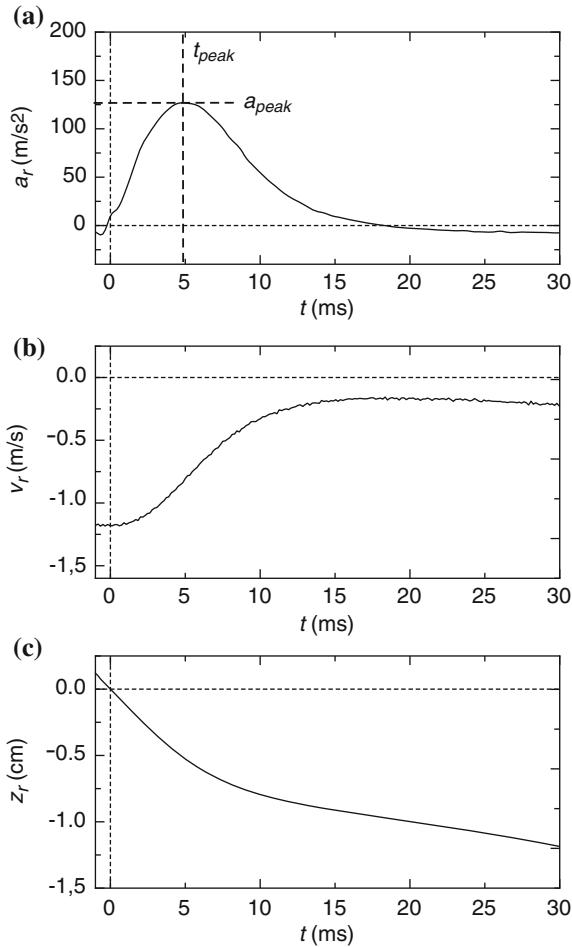
### 2.3 Characterization of Impact

Figure 2.2 shows images before and after the aluminum rod strikes the surface of a deep ( $H = 20.5$  cm) cornstarch and water suspension ( $\phi_0 = 0.49$ ,  $\eta = 1.0$  cP) with impact velocity  $v_0 \sim 1.0$  m/s. Rather than penetrating, as would typically happen during impact into liquid or particles alone, the rod pushes the suspension surface downward, creating a rapidly growing depression whose boundary travels away from the impact site. The absence of splashing indicates that the impact is a highly dissipative since none of the incoming kinetic energy is recovered and redirected to ejecta (indeed the collision in a deep container such as this appears almost “inelastic”). Only after the rod has been slowed to a near stop does it begin to actually sink and penetrate into the suspension. We are concerned with the phenomena before this penetration and sinking occurs.



**Fig. 2.2** Visual characteristics of suspension impact. Images of an aluminum rod before (a) and after (b) it strikes the surface of a cornstarch and water suspension ( $\phi_0 = 0.49$ ,  $\eta = 1.0$  cP) at  $v_0 \sim 1.0$  m/s. Rather than penetrating and creating a splash, the rod seems to push the surface down, creating a large depression that travels radially outward from the impact site. The pockmarked appearance may be a signature of dilation causing particles to poke into the liquid-air interface

Given the complex force laws involved during impact into liquids or particles alone [1–11], one might expect the force law for an object impacting into a suspension to be similarly complex. Surprisingly, this is not the case. Figure 2.3 shows the rod’s instantaneous acceleration  $a_r$  as measured by the embedded accelerometer plotted against time  $t$  (upward acceleration is defined as positive). As the plot shows, the rod’s acceleration starts out at minus  $g$  before impact ( $t < 0$ ). Just after impact, the acceleration steadily grows to some peak value  $a_{peak}$  at time  $t_{peak}$  and then slowly decays to some near-zero or slightly negative value. The existence of peaks in the  $a_r$  versus  $t$  curves indicates that the force law responsible for slowing the rod is a competition between both time-increasing and time-decreasing contributions, and we can use the behavior of these peaks to characterize each impact. As might be guessed from experience, a primary factor that affects the peaking behavior is the impact velocity  $v_0$ ; higher impact velocities lead to larger peaks that occur at earlier times, as shown in Fig. 2.4a. It is also worth noting here that high velocity impacts can lead to incredibly large pressures on the rod face [ $P_{peak} = m_r a_{peak} / (\pi r_r^2)$ ], up to as much as 1 MPa and thus far exceeding the maximum stress ( $\sim 5$  kPa) encountered in steady state shear experiments [24]. For the highest impact velocities (above about 3.0 m/s), the rod begins to penetrate into the suspension. This transition is especially apparent in the plot of  $t_{peak}$  versus  $v_0$  (Fig. 2.4b). Before the transition,  $t_{peak}$  decreases with  $v_0$ , but beyond it actually begins to increase. (Although we do not at present understand the physics of this transition to penetration, we provide some experimental results concerning it in Appendix A and show that it is sensitive to  $r_r$ .)



**Fig. 2.3** Impact dynamics. **a** Acceleration  $a_r$  versus time  $t$  for the aluminum rod striking the surface of a cornstarch and water suspension ( $\phi_0 = 0.49$ ,  $\eta = 1.0$  cP) at impact velocity  $v_0 = 1.18$  m/s. The impact produces a peak of value  $a_{peak}$  occurring at time  $t_{peak}$ , indicating an underlying competition in the force law. **b** Impactor velocity  $v_r$  versus  $t$ , showing impact nearly brings rod to a complete stop before gravity reaccelerates it downwards and it slowly sinks into suspension (not shown). **c** Rod position  $z_r$  versus  $t$

Also in accordance with experience, the impact response is highly sensitive to the particle packing fraction  $\phi_0$ , with more densely packed suspensions leading to higher values of  $a_{peak}$  and smaller values of  $t_{peak}$  (at a given impact velocity  $v_0$ , also shown in Fig. 2.4). In densely packed suspensions, an increase of just a few percent in  $\phi_0$  can cause the peak accelerations to double or triple. This creates practical limitations for conducting experiments. Below  $\phi_0 \sim 0.46$ , the effect becomes so small that it is difficult to detect. At the other extreme, suspensions with packing

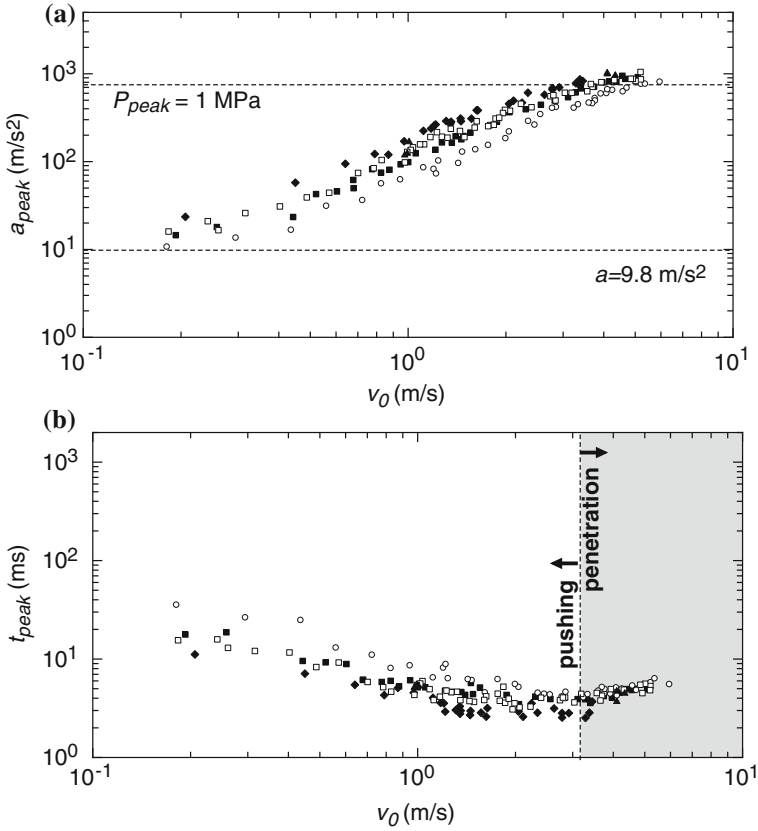


**Fig. 2.4** Parameters affecting peaking behavior. **a** Peak accelerations  $a_{peak}$  versus impact velocity  $v_0$  for experiments with following parameters:  $\eta = 1.0$  cP and  $\phi_0 = 0.46$  (open circles),  $\phi_0 = 0.49$  (solid squares),  $\phi_0 = 0.52$  (solid diamonds),  $\eta = 12.4$  cP and  $\phi_0 = 0.49$  (open squares), and  $\eta = 1.0$  cP and  $\phi_0 = 0.49$  with a water layer approximately 1 cm deep on the suspension surface (solid triangles). **b** Time to peak acceleration  $t_{peak}$  versus impact velocity  $v_0$  with same symbols as in (a). The vertical dashed line indicates the crossover region to the right of which the rod begins to pierce the suspension surface

fractions above  $\sim 0.52$  are so sensitive to perturbations that their relaxation time for reaching a liquid state can take hours. Consequently, our work is restricted to the regime  $0.46 < \phi_0 < 0.52$ .

While the peaking behavior is strongly sensitive to the impact velocity and packing fraction, it is surprisingly insensitive to the properties of the liquid. Changing the viscosity by more than a factor of 10 has no observable effect on the peaks (although it does slow the post-impact sinking behavior). Furthermore, completely removing the effects of surface tension by adding a layer of water ( $\sim 1$  cm deep) to the top of the suspension shows that the response is not associated with particles poking out of the liquid-air interface. As mentioned in Chap. 1, the viscosity of a suspension that

exhibits continuous shear thickening does scale with the suspending liquid viscosity [26–28], while the stresses of a discontinuous shear thickening suspension is limited by surface tension effects [24]. The irrelevance of both viscosity and surface tension reemphasizes that impact response cannot be explained by existing shear thickening models.

## 2.4 Boundary Effects

To see what role, if any, is played by the opposing boundary during impact, we changed the suspension height  $H$  and looked for corresponding changes in the  $a_r$  versus  $t$  curves, as in Fig. 2.5. For the deepest suspension,  $t_{peak} \sim 10$  ms, but a second, weaker peak is just visible near  $t \sim 75$  ms. Lowering  $H$  causes this secondary peak to intensify and move to earlier times. Interestingly, however, the first peak remains largely unchanged. For the smallest  $H$ , a third peak emerges as a consequence of the impulse on the rod being so large that it bounces upward off of the surface, freely accelerates downward at minus  $g$  for a few milliseconds, and then hits the surface again (as indicated in the lowest panel of Fig. 2.5). For the lowest two values of  $H$ , the response becomes dominated by this second peak and the character of impact changes completely. Rather than appearing inelastic, the impact can actually be quite elastic, with as much as 25% of the impactor’s initial speed recovered in the recoil (see Fig. 2.6). Additionally, we see that the coefficient of restitution  $\epsilon$ , defined as the recoil velocity divided by the impact velocity, is largely independent of impact velocity until  $v_0 \sim 3.0$  m/s, i.e. near the transition to the penetration regime.

One might guess that the second peak, which occurs while the rod is still in contact with the suspension surface, might arise from the transmission and reflection of waves to the opposing boundary. If this were the case, then one would expect to see a strong, peak-like signal on the force sensor at the container bottom at half the time of the second peak in the accelerometer. Surprisingly, as the bottom panel of Fig. 2.5 shows, the peak on the force sensor occurs at the same time as the second peak. This is actually a signature of the solidification suspected by Liu et al. [29] and von Kann et al. [30], but these measurements have several key, new implications: first, the primary response (i.e. the original acceleration peak) is not the result of stress transmission to the boundary; second, the suspension does indeed solidify, but the solidification process requires a finite amount of time to propagate through the suspension; third, once solidification reaches the bottom boundary, forces propagate with little delay through the solid-like region back towards the impactor; and fourth, this solid can bear stress and store energy, allowing, for example, the bounce of the impactor.

These implications are more fully appreciated in Fig. 2.7, which shows the force on the rod ( $F_r = m_r a_r$ ) and the force on the container bottom for system parameters ( $H = 11.5$  cm,  $v_0 = 2.0$  m/s,  $\phi_0 = 0.49$  and  $\eta = 1.0$  cP) that prevent the rod from bouncing and separating from the suspension surface (like the bouncing in Fig. 2.5, which removes the solid-coupling between the rod and container bottom). A slow

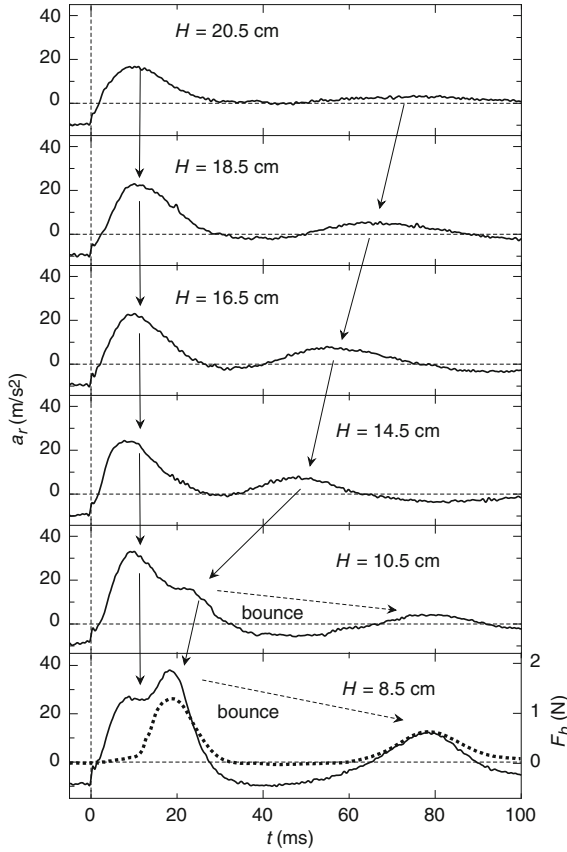


**Fig. 2.5** Effect of lower boundary. Rod acceleration  $a_r$  versus time  $t$  for impact with  $\eta = 1.0\text{cP}$ ,  $\phi_0 = 0.49$ ,  $v_0 = 0.49 \pm 0.04\text{ m/s}$  and suspension fill heights  $H = 20.5, 18.5, 16.5, 14.5, 10.5,$  and  $8.5\text{ cm}$  (top to bottom, as indicated). The dashed line in the bottom panel is the force on the sensor at the container bottom  $F_b$

initial buildup of the force measured on the container bottom  $F_b$  is followed by an abrupt jump (over  $\sim 1.5\text{ ms}$ ) to its maximum value of  $\sim 7\text{ N}$  at  $t \sim 7.5\text{ ms}$ . Before this,  $F_b$  and  $F_r$  show no correspondence. After this, however, it is clear that the spur on the latter part of  $F_r$  has the same shape  $F_b$ . This further indicates that the transmission of stress between the rod at the top of the suspension and the force sensor at the bottom is solid-like. What is more, these data suggest that the solid-like region is concentrated in a column almost directly below the rod, in agreement with the clay-witness experiments of Liu et al. [31]. Noting that the area of the force sensor is  $\sim 1.13\text{ cm}^2$  and, assuming the pressure on the bottom is roughly constant, we estimate that the total force on the rod is recovered over an area  $\sim 10\text{ cm}^2$ . This is much smaller than the full area of the container bottom ( $900\text{ cm}^2$ ), and if we imagine the stress propagates through the suspension in a cone this corresponds to an angle

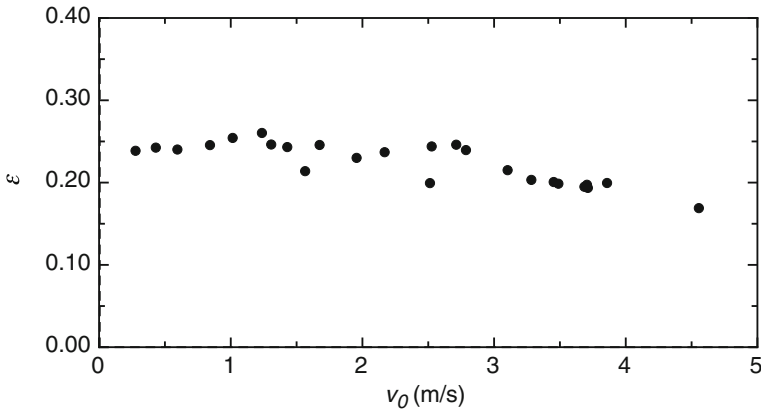


**Fig. 2.6** Restitution coefficient. Coefficient of restitution  $\epsilon \equiv v_{recoil}/v_0$  (where  $v_{recoil}$  is the velocity with which the rod bounces upward off of the surface) for a suspension with  $\phi_0 = 0.49$ ,  $\eta = 1.0\text{cP}$ , and  $H = 8\text{cm}$ . The existence of the bounce indicates that the region of suspension below the rod stores elastic energy just like a solid

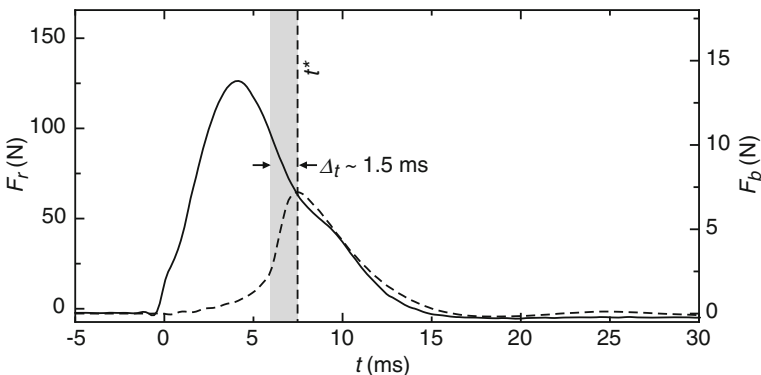


**Fig. 2.7** Details of stress transmission to container bottom. Force on rod  $F_r$  versus time  $t$  (solid curve, left axis) and simultaneously measured force on container bottom directly below rod  $F_b$  versus  $t$  (dashed curve, right axis) for suspension with  $H = 11.5\text{cm}$ ,  $\phi_0 = 0.49$ ,  $\eta = 1.0\text{cP}$  and impact velocity  $v_0 = 2.0\text{m/s}$ . The time of the peak in  $F_b$  (or equivalently, time of 2nd peak in  $F_r$ ) can be interpreted as time required for solid-like growth to reach bottom. The rise time to the peak (especially pronounced for these impact parameters) can be used to show that the width of the solidification front in this realization is approximately  $v_0\Delta t \sim 4\text{mm}$

of about  $10^\circ$  (though this may underestimate the cone angle given that the pressure is presumably highest directly below the rod).

These data suggest that the timing of the 2nd peak in the rod acceleration (or equivalently the timing of the first peak on the force sensor below) can be interpreted as the time  $t^*$  required for the front of a solid-like column to grow from the suspension surface to the bottom boundary. By measuring  $t^*$  at several different  $H$  (as we did in Fig. 2.5), we can plot the trajectory of the solidification front as it

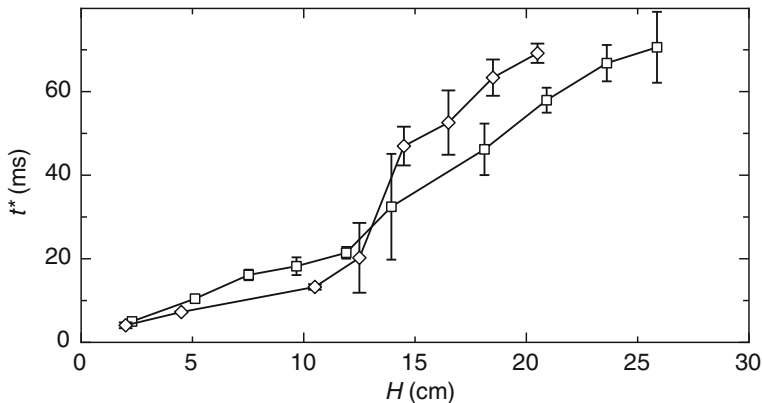


**Fig. 2.8** Trajectory of solidification front. Time of the second peak of the rod’s acceleration  $t^*$  versus suspension fill height  $H$  for impact velocities  $v_0 = 0.49 \pm 0.04$  m/s (*squares*) and  $0.9 \pm 0.1$  m/s (*diamonds*)

develops, as in Fig. 2.8. Close inspection of these data reveals two points. First, higher impact velocities produce fronts that travel with higher initial speeds. Second, these trajectories have the same qualitative features of the rod trajectories, i.e. two straight line regions connected by a soft bend (see for example Fig. 2.3c). What’s more, the timing of the bends in the front trajectories ( $\sim 10$ – $15$  ms) is very close to the timing in the trajectories of the rod itself.

The resemblance of the rod trajectory in Fig. 2.3c and the front trajectory in Fig. 2.8 suggests that the growth of the solid may be related to the displacement of the rod. To test this directly, we plot the size of the solidified region  $h_f$  at  $t^*$  versus the distance travelled by the rod at the same instant  $z_r^*$  in Fig. 2.9 for the same data as in Fig. 2.8. (Note the position of the front below the original surface at  $t^*$  is  $z_f = -H$ . More often, we will refer to the vertical extent of the front  $h_f = H - z_r^*$ .) Doing so collapses the data for the two different impact speeds onto what is nearly a straight line of given by  $h_f = kz_r^*$  with  $k \approx 12.2$ . We define the proportionality constant  $k$  as the *relative front growth rate* of the suspension. Throughout the rest of this thesis, we will refer to  $k$  often as it turns out to be an important parameter for characterizing the suspension behavior.

Going back to Fig. 2.7, we can use the rise time in the force measured on the container bottom to estimate the width of the solidification front. As the figure shows,  $\Delta_t \sim 1.5$  ms. Given that the front crashes into the bottom with the speed of the rod, its width is approximately  $v_r \Delta_t \sim 4$  mm. This shows that, relative to the size of the solidified column or even the size of the rod, the solidification front can be extremely well-defined. (As we will show in this chapter and Appendix B, the front width may depend on both the particle packing fraction and the viscosity of the suspending liquid, though we did not experimentally probe these dependencies in great detail.)

These behaviors are reminiscent of shocks in granular systems above jamming [32, 33] or solidification fronts in supercooled glass-forming liquids [34–37].

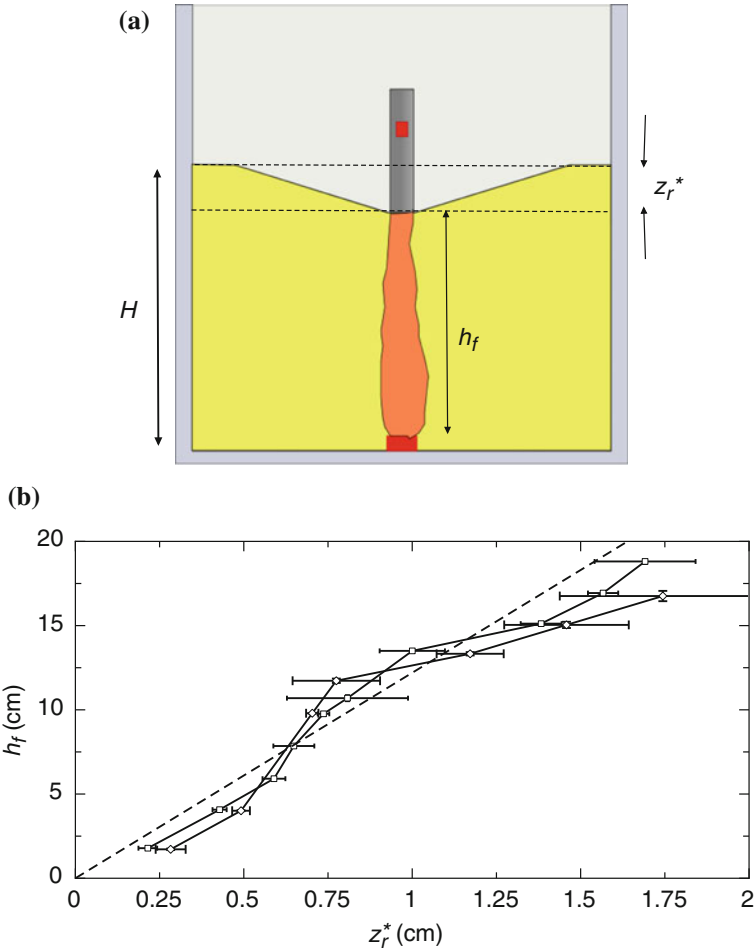


**Fig. 2.9** Solid growth versus rod motion. **a** Cartoon of solid growth below impact site. **b** Vertical extent of solidified region  $h_f$  at instant front hits container bottom plotted against distance below surface travelled by rod at same instant  $z_r^*$  for impact velocities  $v_0 = 0.49^\circ \pm 0.04$  m/s (squares) and  $0.9^\circ \pm 0.1$  m/s (diamonds). Fit is of the form  $h_f = kz_r^*$  with  $k = 12.2$

However, with granular shocks above jamming the front propagates through an already-jammed medium and its speed is governed by elastic energy stored in particles [32, 33]. Although supercooled liquids, like the system here, are initially unjammed, their solidification fronts propagate at a constant, thermodynamically favored speed [37]. The data in Fig. 2.9 show that the fronts here seem to work like a “snowplow”, where the extent of moving snow (suspension) is proportional to how far the shovel (rod) has pushed. As will be shown in this chapter and Chap. 3, this behavior can be tied to jamming of the initially unjammed particle sub-phase as it is compressed by the impacting rod.

## 2.5 Surface Dynamics

The previous section describes what happens directly below the impact site, but it is not immediately apparent how this relates to the features seen on the suspension surface (e.g. Fig. 2.2). Qualitatively, one can argue that the solidified region must cause this surrounding suspension to flow because the lubrication forces described by Eq. 1.2 act as a kind of “glue” between the closely packed particles. In order measure the depression dynamics, we shine a laser sheet across the suspension surface in the field of view of the high speed camera, as in Fig. 2.10. This allows us to make space-time plots of the depth of the surface depression  $z_s$  versus radial coordinate  $r$  and time  $t$ . A typical result is shown in Fig. 2.11. This plot shows more clearly how, for the region to the left of the dashed line in Fig. 2.4, the rod pushes the suspension surface down rather than penetrating into it (note the continuous color spectra across the dashed line indicating the rod/suspension boundary). The plot also shows how regions outside of the depression (i.e. beyond the  $z_s = 0$  mm contour in the blue area) actually swell upward slightly to conserve volume. Interestingly, the trajectory of the  $z_s = 0$  mm contour, like the solid front below the rod, is approximately proportional to the total distance travelled by the rod (and with a proportionality factor very close to the relative front growth rate,  $k = 12.2$ , as indicated by red dashed line in the figure).

## 2.6 Displacements of Suspension Interior

In order to see what happens inside the suspension, we used a C-arm dental X-ray (Orthoscan High Definition Mini C-Arm, Model 1000-0004) to take video (30 frames per second) of a tracer particles in a vertical plane of the suspension interior directly below the impact site, as shown in Fig. 2.12a. (For technical reasons, we had to make a few changes from the setup in Sects. 2.2–2.4. These changes slightly altered the rod dynamics, as discussed in Appendix B. Even so, the salient features of the impact process remained the same.) The tracer particles consisted of small metal objects (e.g. metal spheres, nuts, screws, bolts, nails, and washers) that slowly sank into (and then out of) the field of view of the X-ray apparatus. While the tracers were in the field of view, we released the rod in free-fall from a fixed height allowing it to impact into the suspension ( $v_0 \approx 0.5$  m/s) while simultaneously capturing X-ray video. Given the frame rate was limited to 30 frames per second and the typical impact only lasts  $\sim 20$  milliseconds, these videos give a “before and after” look into the suspension. As the field of view of the X-ray videos was limited to  $\sim 5 \times 5$  cm<sup>2</sup>, we took videos in four separate regions (the boundaries of which can be seen in Fig. 2.12b) and stitched them together.

We used particle imaging velocimetry (PIV) to determine the displacement field of the suspension interior for each video (code in Mathematica written by Justin Burton). Sinking made it difficult to load the tracer particles uniformly, and it was necessary to

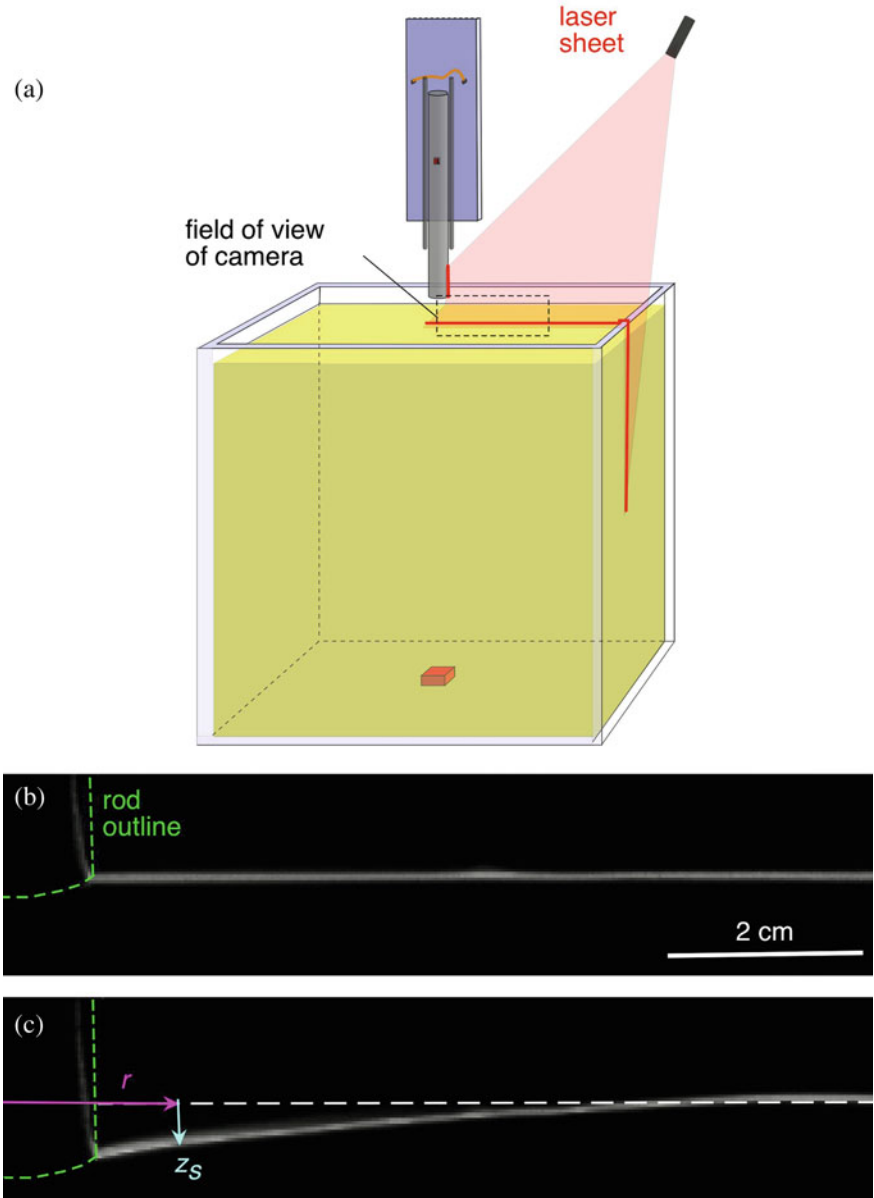


**Fig. 2.10** Laser sheet measurements of surface depression. **a** A laser sheet is used to generate a bright line on the suspension surface in the field of view of the camera. **b** Image of laser line on surface just before impact. Rod is outlined in *green*. **c** Image of laser line on surface about 15 ms after impact

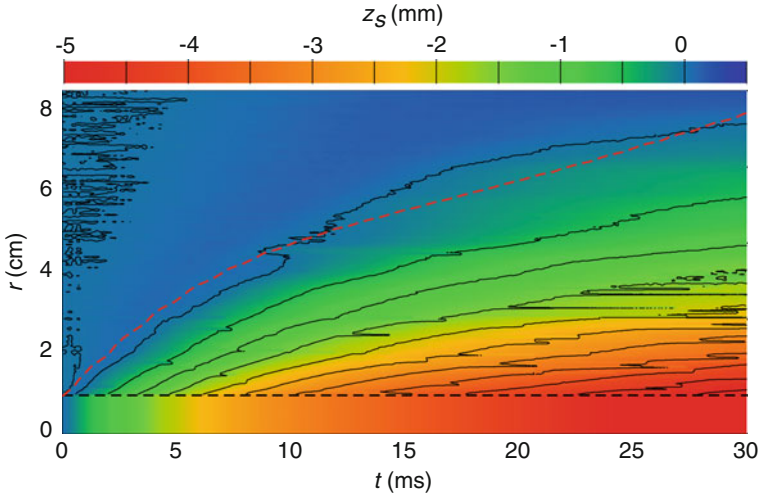


**Fig. 2.11** Space-time plot of surface depression. Depth of surface depression  $z_s$  (*color axis*) versus radial coordinate  $r$  and time  $t$  (with parameters  $\eta = 1.0$  cP,  $\phi_0 = 0.49$ , and  $v_0 = 0.49 \pm 0.01$  m/s). The *blue* part of the figure corresponds to regions outside the conical depression (not there is slight upswell in this region to conserve volume). The *black dashed line* indicates the boundary between the rod and suspension, and the smooth color gradient across this line indicates the rod does not penetrate but instead pushes the surface downward. Contours are drawn for every 1 mm. The *red dashed line* corresponds to the rod trajectory multiplied by factor  $k = 12.2$ , the same factor found for the solid growth below the rod

take several videos in each field of view, ignore the PIV data corresponding to regions that lacked particles, and then average the results from different videos together to fill in the gaps. A final displacement field is shown in Fig. 2.13. The first striking feature of these data is the large region of suspension that moves downward, extending approximately 6 cm below the rod and 5 cm to the side (red to green in the figure). What makes this especially remarkable is that all of this movement is a result of the rod moving a mere 5 mm below the original surface level. To the side of this downward moving region, the PIV data make it clear that the suspension flows upward. As mentioned in Sect. 2.4, where the same upward motion was seen with the laser sheet measurements (Fig. 2.11), this must occur because the suspension as a whole is incompressible and the vacated volume of the depression has to be compensated for by an upswell on the periphery. These observations give a quick, qualitative answer to how the rod is slowed down during impact. In brief, even a very small amount of rod motion creates a vastly larger region of flow in the suspension. The mechanism for the slowing of the impactor is the transfer of momentum to this growing, moving region.

The PIV data also provide a second opportunity to quantitatively confirm the relationship between the growth of the solid front relative to the displacement of the rod. We start with the following simple assumption: if a segment of suspension has been solidified, it moves rigidly with the rod, whereas if it has not been solidified then

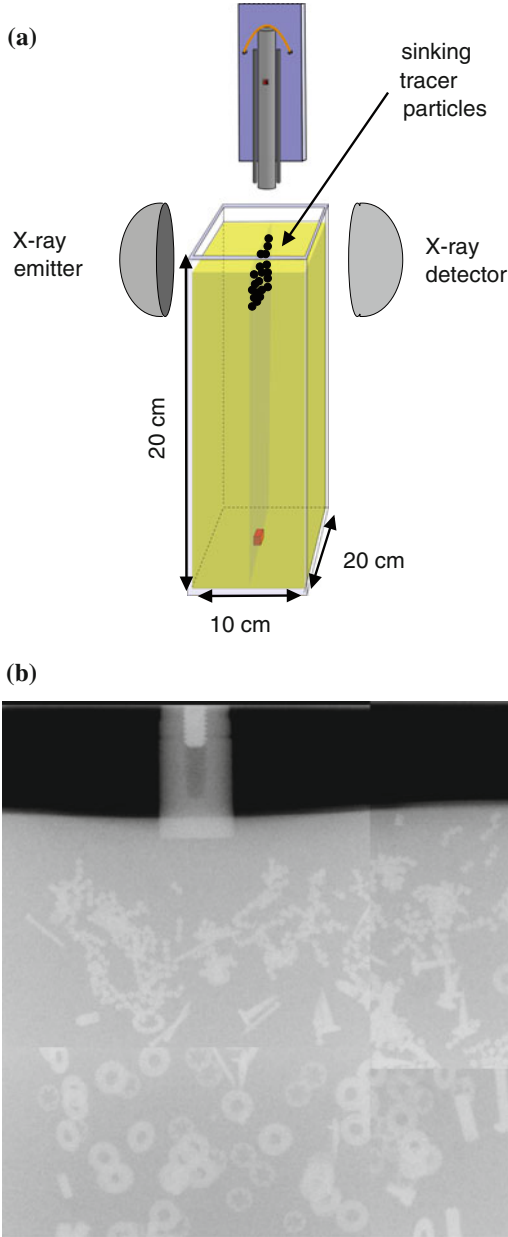


**Fig. 2.12** X-ray measurements of interior dynamics. **a** X-ray emitter shines through suspension toward detector. The plane of the suspension directly below the impacting rod is laden with metal particles to act as tracers in the X-ray video. **b** X-ray image of tracer particles in the suspension interior just after rod strikes the surface at  $v_0 \approx 0.5$  m/s. Note that the container extends equally to the *right* and *left* of the rod, but imaging was performed primarily to the *right* side, hence the asymmetry in the figure

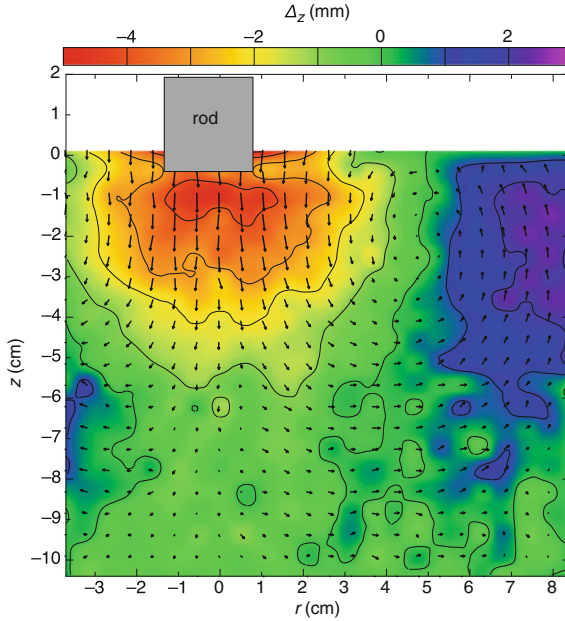


**Fig. 2.13** Suspension interior displacement field. Displacement field of suspension in a plane directly below impact site calculated via particle imaging velocimetry (PIV) of X-ray images taken before and after impact. The large downward moving region (*red to green* in the figure), which extends nearly 6 cm below and away from the rod, develops after the rod itself moves only  $\sim 5$  mm. Outside of this downward moving region, the suspension moves upward to conserve volume globally

it does not move all. If the rod moves a total distance  $|z_r|$  beyond the original surface between two X-ray images, then the edge of the front will reach a depth  $|z_r|(k + 1)$  below the surface, so beyond this depth all displacements  $\Delta_z$  should be zero. Above this depth, a segment of the solidified column at depth  $|z|$  will move however far the rod moved after it was picked up, i.e.

$$|\Delta_z| = |z_r| - \frac{|z|}{k + 1}. \quad (2.2)$$

In Fig. 2.14 we plot the vertical displacements  $|\Delta_z|$  of the suspension below the rod as a function of  $|z|$ . The data have the qualitative shape predicted by Eq. 2.2, starting out by decreasing linearly and then coming to (nearly) zero displacement. Fitting the linear region to Eq. 2.2, we find  $|z_r| = 5.0 \pm 0.2$  mm and  $k = 13.1 \pm 0.9$ , very close to the value found from varying the suspension height  $H$  (Fig. 2.9).

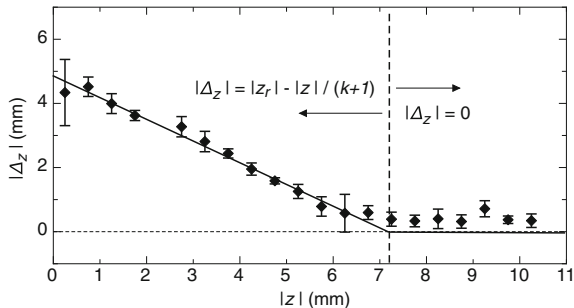


**Fig. 2.14** Vertical displacements of suspension directly below impact site. Experimental data (*diamonds*) and model prediction (*black line*). As discussed in the text, the “snowplow” model for solidification predicts that the displacements should be zero beyond the distance  $|z| = (k + 1)|z_r|$  and should decrease like  $|\Delta_z| = |z_r| - |z|/(k + 1)$  before this distance. Fitting to this proposed form gives the relative front growth rate  $k = 13.1 \pm 0.9$ , close to the value found in Sect. 2.2

## 2.7 Added Mass Model for Impact

The results of the previous three sections paint a picture in which the seed of the suspension response to impact is the dynamic growth of the solid below the impact site. As this solid grows and is forced to move with the rod, it causes flow in the surrounding, still liquid-like suspension. The interplay between this growing region of moving suspension and the slowing of the rod is the competition mechanism responsible for the observed peaks in the rod deceleration. We can capture the essence of this behavior using the concept of added mass, as is frequently done for surface impact in regular liquids [2, 4, 38]. The key idea is to think of the impact as an inelastic collision between the rod and a growing mass,  $m_a$ . The rod dynamics are captured by force balance:

$$(m_r + m_a)a_r = \frac{dm_a}{dt}v_r + F_{ext}. \quad (2.3)$$

where  $F_{ext}$  accounts for other forces not associated with momentum transfer to the added mass, e.g. the force of gravity on the rod  $m_r g$  and the buoyant force from the displaced liquid in the depression (from Fig. 2.5, this is  $\sim 1/3\pi g(r_r + k|z_r|)^2|z_r|$ ). With normal liquids,  $m_a$  is typically limited by the density of the liquid and the size of the impactor, for example,  $m_a < C(4/3)\pi\rho_l(r_r)^3$  for the impact of a disk of radius  $r_r$  into a liquid of density  $\rho_l$  [2]. The factor  $C$  is the “added mass coefficient” and accounts for the fact that the liquid does not actually move like a solid object (consequently,  $C$  is typically less than 1). The suspension is capable of responding so dramatically because the solidification below the rod leads to rapid, effectively unlimited growth of  $m_a$ . We can estimate its size from Figs. 2.9 and 2.11, which

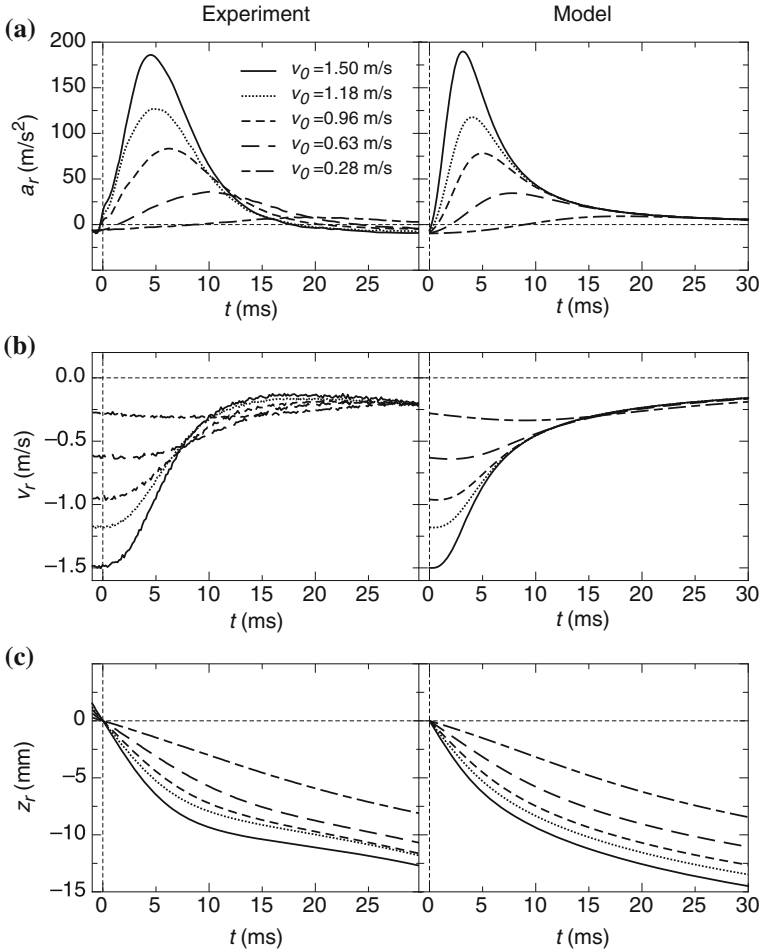


**Fig. 2.15** Comparison of added mass model with experimental results. Experimental (*left column*) and numerical (*right column*) results for acceleration (**a**), velocity (**b**) and position (**c**) of rod impacting into suspension with  $\eta = 1.0\text{cP}$ ,  $\phi_0 = 0.49$ , and impact velocities  $v_0 = 1.50\text{ m/s}$  (*solid line*),  $1.18\text{ m/s}$  (*dots*),  $0.96\text{ m/s}$  (*small dash*),  $0.63\text{ m/s}$  (*large dash*) and  $0.28\text{ m/s}$  (*alternating small/large dash*). Numerical results are Mathematica solutions to Eqs. 2.3 and 2.4 with parameters  $m_r = 0.368\text{ kg}$ ,  $k = 12.5$ ,  $r_r = 0.93\text{ cm}$  and  $\rho_s = 1295\text{ kg/m}^3$  and initial conditions  $v_r(0) = -v_0$  and  $z_r(0) = 0$

show that the impact creates substantial flow in a region that extends  $k|z_r|$  below and radially away from the rod. Approximating these points as bounding a cone-like region gives  $m_a$  the form:

$$m_a = C \frac{1}{3} \rho_s \pi (r_r + k|z_r|)^2 k|z_r|, \quad (2.4)$$

where  $\rho_s$  is the density of the suspension. Using this in Eq. 2.3 with the initial conditions  $v_r(0) = -v_0$  and  $z_r(0) = 0$  allows us to solve numerically for the rod dynamics. With the average measured value for the relative front growth rate ( $k = 12.5$ ) and leaving the coefficient  $C$  as the only adjustable parameter, this minimal model reproduces the important features impact response surprisingly well over the whole range of initial velocities tested (Fig. 2.15). We find the best agreement for  $C \approx 0.37$ , similar to what is encountered for disk impact into regular liquids [4]. (In Appendix C, we extract  $m_a$  directly from our data and confirm the scaling with  $|z_r|$  as given by Eq. 2.3. In Appendix D, we show how similar behaviors can arise if the growing solid column below the rod experiences viscous drag from the surrounding suspension.)

## References

1. M. Shiffman, D.C. Spencer, The force of impact on a cone striking a water surface (vertical entry). *Commun. Pur. Appl. Math.* **4**(4), 379–417 (1951)
2. C.E Brennen, A review of added mass and fluid inertial forces. Report to the Department of the Navy (CR 82.010) (1982)
3. A.A. Korobkin, V.V. Pukhnachov, Initial stage of water impact. *Annu. Rev. Fluid Mech.* **20**(1), 159–185 (1988)
4. J.W. Glasheen, T.A. McMahon, Vertical water entry of disks at low froude numbers. *Phys. Fluids* **8**, 2078–2083 (1996)
5. R. Bergmann, D. Van Der Meer, S. Gekle, A. Van Der Bos, D. Lohse, Controlled impact of a disk on a water surface: cavity dynamics. *J. Fluid Mech.* **633**, 381–409 (2009)
6. M. Ambroso, R. Kamien, D. Durian, Dynamics of shallow impact cratering. *Phys. Rev. E* **72**(4), 041305 (2005)
7. M. Hou, Z. Peng, R. Liu, K. Lu, C. Chan, Dynamics of a projectile penetrating in granular systems. *Phys. Rev. E* **72**(6), 062301 (2005)
8. H. Katsuragi, D.J. Durian, Unified force law for granular impact cratering. *Nat. Phys.* **3**(6), 420–423 (2007)
9. D.I. Goldman, P. Umbanhower, Scaling and dynamics of sphere and disk impact into granular media. *Phys. Rev. E* **77**(2), 021308 (2008)
10. S. Von Kann, S. Joubaud, G.A. Caballero-Robledo, D. Lohse, D. Van Der Meer, Effect of finite container size on granular jet formation. *Phys. Rev. E* **81**(4), 041306 (2010)
11. J.R. Royer, B. Conyers, E.I. Corwin, P.J. Eng, H.M. Jaeger, The role of interstitial gas in determining the impact response of granular beds. *Europhys. Lett.* **93**, 28008 (2011)
12. N.J. Wagner, J.F. Brady, Shear thickening in colloidal dispersions. *Phys. Today* **62**(10), 27–32 (2009)
13. D.R. Foss, J.F. Brady, Structure, diffusion and rheology of brownian suspensions by stokesian dynamics simulation. *J. Fluid Mech.* **407**(1), 167–200 (2000)
14. J.R. Melrose, R.C. Ball, Continuous shear thickening transitions in model concentrated colloids: The role of interparticle forces. *J. Rheol.* **48**, 937–961 (2004)
15. B.J. Maranzano, N.J. Wagner, Flow-small angle neutron scattering measurements of colloidal dispersion microstructure evolution through the shear thickening transition. *J. Chem. Phys.* **117**, 10291–10303 (2002)
16. D.P. Kalman, N.J. Wagner, Microstructure of shear-thickening concentrated suspensions determined by flow-USANS. *Rheol. Acta* **48**(8), 897–908 (2009)

17. X. Cheng, J.H. McCoy, J.N. Israelachvili, I. Cohen, Imaging the microscopic structure of shear thinning and thickening colloidal suspensions. *Science* **333**(6047), 1276–1279 (2011)
18. A. Fall, N. Huang, F. Bertrand, G. Ovarlez, D. Bonn, Shear thickening of cornstarch suspensions as a reentrant jamming transition. *Phys. Rev. Lett.* **100**, 018301 (2008)
19. E. Brown, H. Jaeger, Dynamic jamming point for shear thickening suspensions. *Phys. Rev. Lett.* **103**(8), 086001 (2009)
20. E. Brown, N.A. Forman, C.S. Orellana, H. Zhang, B.W. Maynor, D.E. Betts, J.M. Desimone, H.M. Jaeger, Generality of shear thickening in dense suspensions. *Nat. Mater.* **9**(3), 220–224 (2010)
21. E.E. Bischoff White, M. Chellamuthu, J.P. Rothstein, Extensional rheology of a shear-thickening cornstarch and water suspension. *Rheol. Acta* **49**(2), 119–129 (2010)
22. C.S. Orellana, J. He, H.M. Jaeger, Electrorheological response of dense strontium titanyl oxalate suspensions. *Soft Matter* **7**(18), 8023–8029 (2011)
23. A. Fall, F. Bertrand, G. Ovarlez, D. Bonn, Shear thickening of cornstarch suspensions. *J. Rheol.* **56**, 575–592 (2012)
24. E. Brown, H.M. Jaeger, The role of dilation and confining stresses in shear thickening of dense suspensions. *J. Rheol.* **56**(4), 875–924 (2012)
25. F. Merkt, R. Deegan, D. Goldman, E. Rericha, H. Swinney, Persistent holes in a fluid. *Phys. Rev. Lett.* **92**(18), 184501 (2004)
26. W.H. Boersma, J. Laven, H.N. Stein, Shear thickening (dilatancy) in concentrated dispersions. *AIChE J.* **36**(3), 321–332 (1990)
27. E. Brown, H. Zhang, N.A. Forman, B.W. Maynor, D.E. Betts, J.M. DeSimone, H.M. Jaeger, Shear thickening and jamming in densely packed suspensions of different particle shapes. *Phys. Rev. E.* **84**(3), 031408 (2011)
28. W.J. Frith, P. d’Haene, R. Buscall, J. Mewis, Shear thickening in model suspensions of sterically stabilized particles. *J. Rheol.* **40**, 531–549 (1996)
29. B. Liu, M. Shelley, J. Zhang, Focused force transmission through an aqueous suspension of granules. *Phys. Rev. Lett.* **105**(18), 188301 (2010)
30. S. von Kann, J.H. Snoeijer, D. Lohse, D. van der Meer, Nonmonotonic settling of a sphere in a cornstarch suspension. *Phys. Rev. E* **84**(6), 060401 (2011)
31. A.J. Liu, S.R. Nagel, Jamming is not just cool any more. *Nature* **396**(6706), 21–22 (1998)
32. L. Gómez, A. Turner, M. Van Hecke, V. Vitelli, Shocks near jamming. *Phys. Rev. Lett.* **108**(5), 058001 (2012)
33. L. Gómez, A. Turner, V. Vitelli, Uniform shock waves in disordered granular matter. *Phys. Rev. E* **86**(4), 041302 (2012)
34. M.D. Ediger, C.A. Angell, S.R. Nagel, Supercooled liquids and glasses. *J. Phys. Chem.* **100**(31), 13200–13212 (1996)
35. M. Papoular, Dense suspensions and supercooled liquids: dynamic similarities. *Phys. Rev. E* **60**, 2408–2410 (1999)
36. P.G. Debenedetti, F.H. Stillinger, Supercooled liquids and the glass transition. *Nature* **410**(6825), 259–267 (2001)
37. D.J. Graham, P. Magdolinis, M. Tosi, Investigation of solidification of benzophenone in the supercooled liquid state. *J. Phys. Chem.* **99**(13), 4757–4762 (1995)
38. M. Moghisi, P.T. Squire, An experimental investigation of the initial force of impact on a sphere striking a liquid surface. *J. Fluid Mech.* **108**, 133–146 (1981)



<http://www.springer.com/978-3-319-09182-2>

Impact-Activated Solidification of Cornstarch and Water  
Suspensions

Waitukaitis, S.R.

2015, XVIII, 88 p. 53 illus., 20 illus. in color., Hardcover

ISBN: 978-3-319-09182-2